Effect of a new synthetic bubble model on forces in simulations of two-phase flows in tube bundles

Laurent De Moerloose[a,*], Axel Bral[a], Toon Demeester[a], Michel De Paepe[a,b], Joris Degroote[a,b]

[a] *Department of Electromechanical, Systems and Metal Engineering, Faculty of Engineering and Architecture, Ghent University, Sint-Pietersnieuwstraat 41-B4, 9000 Ghent, Belgium*
[b] *FlandersMake@UGent corelab EEDT MP, Belgium*

Abstract

In this paper, the influence of the phase distribution imposed as an inlet boundary condition in a two-phase flow simulation is investigated. Firstly, a new inlet model is proposed which defines a transient inlet boundary condition to be applied in a subsequent Eulerian simulation, more specifically using the Volume-Of-Fluid method. This inlet model is aimed at generating large gas bubbles, making a Lagrangian approach less applicable. The new model, which is coined the "Synthetic Bubble Model" (SBM), generates a transient inlet condition with large gas bubbles such that there is no need for bubble creation through break-up of a continuous gas jet in a long inlet region upstream of the region of interest, which results in a smaller computational mesh. This model is applied on a 5-by-3 tube bundle subjected to an axially flowing air/water mixture and compared to a simulation with a precursor-domain in which bubbles are created by break-up of air jets imposed at the inlet. Compared to the precursor domain simulations, the SBM is both faster and more or equally accurate. Secondly, a tube bundle subjected to two-phase cross-flow is modelled. It is shown that the SBM yields better correspondence with the experimental force data than a steady inlet condition, in this case without addition of a precursor-domain (yielding a similar computational time for both simulations).

Keywords: computational fluid dynamics, two-phase flow, flow-induced vibrations, tube bundle

1. Introduction

With the increase of computational power, numerical modelling of two-phase flow has gained importance in the last two decades. On the one hand, some studies focus on accurate numerical modelling of the bubble shape. In that

*Corresponding author. Tel. +32 9 264 32 97, Fax. +32 9 264 35 90
Email address: laurent.demoerloose@ugent.be (Laurent De Moerloose)

case, it is customary to start from a bubble which is already present inside the domain (Denner and van Wachem (2014); Karnakov et al. (2020)). On the other hand, some numerical studies start from the assumption that only relatively small bubbles occur in a continuous liquid flow, for which typically Eulerian-Lagrangian modelling (Gouesbet and Berlemont (1999)) is appropriate.

The focus of this research is the inlet modelling of two-phase flow with multiple large bubbles. These flows are important as they cause the largest forces in tube bundles (Nakamura et al. (1995)). However, the aforementioned methods are less applicable for these large bubbles. On the one hand, accurate modelling of the interface curvature is not required and therefore encompasses an unnecessary computational cost. On the other hand, in the Eulerian-Lagrangian approach, bubble interaction, impact or shape change should be modelled explicitly, e.g. based on coalescence criteria (Chesters and Hofman (1982)), but this is only done in a limited number of studies. One example is the work by Trapp (1993), who successfully applied an Eulerian-Lagrangian framework to calculate bubble growth and changing flow topology, but the pressure drop, bubble velocity and forces on the surrounding or immersed tubes have not been validated. Moreover, a Lagrangian model for the bubbles is closed with semi-empirical models for lift and drag forces (Selima et al. (2018)) which are typically not sufficiently accurate for large air structures such as encountered in slug or intermittent flow. Some attempts have been made to increase the accuracy of such closure models in an Eulerian-Lagrangian framework (Parmar et al. (2010); Akiki et al. (2017)), but these have not been tested on large air structures of arbitrary form at this point, whereas non-spherical bubble shapes appear regularly in axial flow through a tube bundle (Liu et al. (2018)).

This leads to the conclusion that the Eulerian-Lagrangian approach is less suitable than the so-called one-fluid models like the Volume-Of-Fluid (VOF) method when investigating two-phase flows with large bubbles. A one-fluid calculation requires a long precursor domain if steady gas jets are imposed at the inlet. These jets need to break up to form a realistic flow field with large bubbles (Alkhalidi and Amano (2015)). In this paper, a new model is proposed which defines a transient inlet boundary condition with bubbles of varying size occurring at a variable location in space and time. This novel approach is coined the "Synthetic Bubble Model" (SBM). To the author's knowledge, no method described in literature efficiently generates such large bubbles with a (uniform) distribution in size and location. The newly-proposed SBM allows the definition of spherical bubbles of variable size at a varying time instant and at a stochastically determined location on the inlet face. The transient inlet boundary condition is to be applied in a subsequent Computational Fluid Dynamics (CFD) simulation.

The novel model definition is specifically aimed at external flow applications, although it is also applicable to internal flow. However, in internal flow examples, i.e. pipe flow, it is reasonably straightforward to introduce stratified or slug flow at the inlet. The former does not require a transient condition whereas the latter can be modelled with a periodic sequence of air bubbles and water slugs, as was done in previous work (De Moerloose and Degroote (2020)).

Furthermore, the spatial bubble distribution of bubbles in pipe flow is naturally limited by the tube diameter. By contrast, the definition of a transient inlet boundary condition in external flow applications is more challenging due to the larger available space and the typical lack of temporal periodicity, which is why the SBM is only tested in external flow cases.

Firstly, the algorithm will be discussed in Section 2. After the description of the CFD model in Section 3, the performance of the SBM will be evaluated on a test case containing a square 5-by-3 tube bundle subjected to an axially flowing air/water mixture. The tube diameter and array pitch match the experiments of Ren et al. (2018) and Liu et al. (2018). A simulation using the boundary condition defined with the SBM is compared to two precursor domain calculations in Section 4. Finally, the model will be applied to a staggered tube bundle subjected to cross-flow and compared to empirical data of Zhang et al. (2007) in Section 5.

2. Description of the Synthetic Bubble Model (SBM)

In this section, a new model is proposed to generate a transient inlet boundary condition to be used in a subsequent Volume-Of-Fluid simulation. The so-called Synthetic Bubble Model (SBM) introduces spherical bubbles of variable size which are stochastic in space and time. Firstly, the concept behind the model is described. Afterwards, the algorithm is discussed in more detail. Additionally, the complete code is published online on the following website: `https://github.com/ldmoerlo/InletModelling_VOF`.

2.1. Concept

The idea behind the model is as follows. The numerical domain to be used in the subsequent CFD calculation has to be defined before applying the SBM. The first step of the model is the construction of a virtual pre-domain. Inside the virtual pre-domain, no CFD simulation is performed. Instead, gas bubbles are distributed in the pre-domain during execution of the SBM. The transient boundary condition imposed at the inlet of the CFD domain is the result of cutting the pre-domain with a plane that shifts one cell in each modelled time step and imposing the values on this cutting plane at the inlet of the actual domain.

The virtual pre-domain is created by extruding the inlet face mesh perpendicular to the CFD domain, as sketched in Figure 1. In case of a two-dimensional inlet boundary, the virtual pre-domain is three-dimensional. Inside the pre-domain, the face mesh on any plane parallel to the inlet boundary plane is an exact copy of the inlet boundary face mesh. The cell size in the normal direction is governed by the product of the flow velocity U and the time step used in the model Δt_{model}. The following discussion will assume the introduction of an air/water mixture, but naturally any type of gas/liquid mixture can be used.

Initially, the entire pre-domain is filled with water: all cells have an α_w-value equal to 1, with α_w being the cell volume fraction of water. The model will then

choose from a probability distribution a value for the bubble radius R_g - within certain limits which will be discussed later - and a location in space and time for the bubble center. This corresponds to choosing a cell center located inside the pre-domain as the new bubble's center. For all cells of the pre-domain, it is subsequently verified whether the cell center is located inside the theoretical bubble. If so, the α_w-value of the corresponding cell is set to zero. The bubble is completely defined after looping over all cells. The amount of gas that is added is determined from the cell volumes and the model can move on to the introduction of a new bubble. This cycle repeats until a certain user-specified amount of air has been introduced in the pre-domain. Consequently, the pre-domain will only consist of α_w-values equal to 0 or 1. The interface of the bubble is hence not exactly modelled. This could be improved by allowing the definition of intermediate α_w-values, but this is not done because the bubbles of interest span more cells than shown in Figure 1, which reduces the discrepancy with the exact spherical shape. Furthermore, numerical diffusion of the liquid-gas interface during the CFD-calculation occurs very rapidly, rendering a more accurate interface representation pointless. Naturally, the algorithm calculates how much air was exactly introduced during each iteration; each bubble will therefore not contain the exact amount of air as anticipated beforehand, but the total amount of air to be introduced will be attained up to a user-set tolerance.

2.2. Algorithm

The new model defines such a transient inlet condition for an arbitrarily long time duration, which the user imposes by setting a start time t_{start} and an end time t_{end}. Additionally, the four most important user parameters are: U, Δt_{model}, m_g and t_{unit}. U is the flow velocity and Δt_{model} is the time step to be used in the SBM. Together, these parameters determine that the smallest bubble that can be modelled is $U\,\Delta t_{model}$ long in the direction normal to the inlet face. Slip between phases is not taken into account and therefore the air and water enter the domain at the same speed and in the direction of the inlet face normal.

To quantify the amount of air to be introduced, the parameter m_g quantifies the mass of air to be introduced during a time interval t_{unit}, up to a user-defined tolerance ϵ_{mg}. This "unit" time interval has to be smaller than or equal to the total flow time and the ratio between both has to be an integer. The total flow time is thus divided in a number of intervals with duration t_{unit}, in which the desired mass input m_g is introduced. This significantly reduces the computational time as the algorithm loops only over the cells of the pre-domain inside one of these intervals whenever a new bubble is defined. Coincidently, as smaller values for t_{unit} limit the available number of locations where a bubble can exist, it is more likely that a more homogeneous distribution of bubbles is achieved, while large values allow the occurrence of zones with large or small concentrations of air.

Algorithm 1 shows the principle behind the SBM. The variable α_w at spatial location corresponding to the face with ID i and in the timestep j is stored in

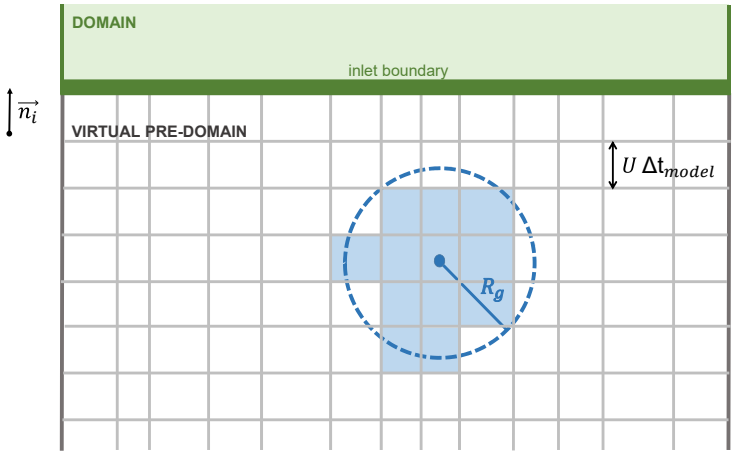

Figure 1: Sketch showing the introduction of a spherical air bubble in the virtual pre-domain defined by the model. The vector $\vec{n_i}$ denotes the normal at the inlet boundary, pointing towards the CFD domain (shown in green). The virtual pre-domain mesh results from sweeping the domain's inlet face mesh in the normal direction. The normal cell size in the pre-domain is equal to $U\Delta t_{model}$. A bubble (shown in dark blue) is placed with its center at a cell center inside the pre-domain and with a radius R_g. The value of α_w of all cells with centers located inside the bubble is set to 0 (these cells are shown in light blue). Uncoloured cells have $\alpha_w = 1$.

matrix element $A_{i,j}$; consequently, $A \in \mathbb{R}^{N_{faces} \times N_{steps}}$. Index i represents the unique ID given to each face located at the inlet and ranges from 0 till the number of cells at the inlet N_{faces} minus one. For a face i, the face area is denoted with S_i. N_{steps} denotes the total number of time steps to be modelled and is equal to $(t_{end} - t_{start})/\Delta t_{model}$. As such, each element $A_{i,j}$ can be interpreted as the α_w-value in a virtual cell $C_{i,j}$, which is constructed from the inlet face i and has a length $U\,\Delta t_{model}$ in the direction normal to the inlet face.

Initially, all elements $A_{i,j}$ are set to one, after which air bubbles are introduced at specific locations in time and space by setting $A_{i,j} = 0$ in the corresponding matrix locations. Currently, the bubbles are spherical, but the model is constructed in such a way that other shapes are straightforward to implement. The values of the bubble radius and center location are chosen from a uniform probability distribution, which is changeable in future work. Overall, a bubble $\mathbb{B}$ is defined by three parameters: the location of the bubble center in space (i_c) and in time (j_c) and the bubble size (m_b). Each of these variables are chosen at the start a new iteration. The bubble size m_b is limited by a lower bound equal to the minimum of the parameter m_{min} and the still available amount of air $m_g - m_{def}$ and an upper bound equal to the minimum of the parameter m_{max} and the still available amount of air $m_g - m_{def}$, where m_{def} is a variable which keeps track of the mass of air already introduced in previous iterations.

In Algorithm 1, the bubble shape, size and location are chosen from a probability distribution, after which it is checked for each possible location in space i and time j whether the cell center $C_{i,j}$ falls inside the new bubble. The user can decide whether a newly-defined bubble can intersect with a previously introduced bubble (which is checked on line 1.24 based on the value of $A_{i,j}$) and whether a bubble can intersect with a wall (which is checked on line 1.33 based on the value of $m_{covered}$) by setting the boolean variables *allowIntersectBubble* and *allowIntersectWall*, respectively. Finally, if the newly-defined bubble complies with all the requirements, the matrix A is updated and the amount of air that was introduced in this iteration m_{iter} is added to the amount of air that was introduced in earlier iterations m_{def}. If one or more criteria are not met, the iteration is stopped and new bubble parameters (i_c, j_c, m) are picked in a subsequent iteration. Clearly, choosing an excessively high m_g or low t_{unit} may lead to insufficient space to define all required bubbles and would therefore put the SBM into an infinite loop. Hence, a counter N_{fail} keeps track of the number of consecutive failed iterations. If this counter reaches a certain hard-coded value, i.e. 1000, the operation is stopped and the user should review the specified settings. Finally, $\epsilon_{covered}$ is a tolerance which takes into account that the spherical shape of the bubble cannot be exactly reproduced on the grid and that the target mass m_b will therefore be different from the actually introduced mass m_{iter} even if the bubble does not intersect with the wall.

The model was defined in Python and was coupled to the software package OpenFOAM®, initially for version 4.1, but it has been tested successfully for version 6 as well (see Section 5). Nevertheless, the solver-specific part of the code is limited to reading the coordinates and face areas of the inlet boundary on the

Algorithm 1 The Synthetic Bubble Model (SBM)

$k = 0$
$N_{unit} = (t_{end} - t_{start}) / t_{unit}$
for $i \in [0, N_{faces} - 1]$, $j \in [0, N_{steps} - 1]$ **do**
    $A_{i,j} = 1$
end for
while $k < N_{unit}$ **do**
    $m_{def} = 0$
    $N_{fail} = 0$
    while $m_g - m_{def} > \epsilon_{mg}$ **and** $N_{fail} < 1000$ **do**
        Pick $i_c \in [0, N_{faces} - 1]$
        Pick $j_c \in [k\, N_{unit}\ t_{unit}/\Delta t_{model}, (k+1)\, N_{unit}\ t_{unit}/\Delta t_{model} - 1]$
        Pick $m_b \in [\min(m_{min}; m_g - m_{def}), \min(m_{max}; m_g - m_{def})]$
        $T = A$
        $m_{covered} = 0$
        $m_{iter} = 0$
        iterationSuccessful = True
        for $i \in [0, N_{faces} - 1]$,
         $j \in [k\, N_{unit}\, t_{unit}/\Delta t_{model}, (k+1)\, N_{unit}\, t_{unit}/\Delta t_{model} - 1]$ **do**
            if cell $C(i,j)$ inside new bubble $\mathbb{B}(i_c, j_c, m_b)$ **then**
                if $A_{i,j} = 1$ **then**
                    $T_{i,j} = 0$
                    $m_{iter} = m_{iter} + \rho_g\, U\, S_i\, \Delta t_{model}$
                    $m_{covered} = m_{covered} + \rho_g\, U\, S_i\, \Delta t_{model}$
                else if $A_{i,j} = 0$ **and** *allowIntersectBubble* **then**
                    $m_{covered} = m_{covered} + \rho_g\, U\, S_i\, \Delta t_{model}$
                else
                    N_{fail}=N_{fail}+1
                    iterationSuccessful = False
                    break
                end if
            end if
        end for
        if $m_{covered} < m_b - \epsilon_{covered}$ **and not**(*allowIntersectWall*) **then**
            N_{fail}=N_{fail}+1
            iterationSuccessful = False
        end if
        if *iterationSuccessful* **then**
            $A = T$
            $m_{def} = m_{def} + m_{iter}$
            $N_{fail} = 0$
        end if
    end while
    $k = k + 1$
end while

one hand and the final conversion of the newly-defined boundary condition to a format readable by OpenFOAM® on the other hand. The latter is done by using the *timeVaryingMappedFixedValue*-boundary condition in OpenFOAM®. Contrariwise, the definition of the pre-domain and therefore the inlet boundary condition is independent of the flow solver and can be used in any flow solver using the VOF-method. Note that the time step used in the OpenFOAM® simulation does not have to equal the time step used in the model (Δt_{model}); the *timeVaryingMappedFixedValue*-condition interpolates between subsequent time instants for which the inlet condition is explicitly modelled.

3. Computational Fluid Dynamics (CFD)

In the following paragraphs, two different cases will be tested in the open-source finite volume software package OpenFOAM®, more specifically using the solver *interFoam*. This solver assumes incompressible, immiscible and isothermal phases. In the case of externally flowing air-water mixtures at low Mach numbers and at ambient conditions, this assumption is reasonable. The solver has been validated over a range of applications (Deshpande et al. (2012); Damián (2013); Shuard et al. (2016); Larsen et al. (2019)). For the most part, the modelling parameters are similar in all cases. These are described in this section. The settings that vary from case to case will be mentioned explicitly in the corresponding sections.

For all CFD simulations, the Volume-Of-Fluid (VOF) method as first described by Hirt and Nichols (1981) is adopted. This is an Eulerian one-fluid model in which the mass and momentum equation are defined with the mixture density ρ_m and viscosity μ_m, i.e.:

$$\rho_m = \alpha_w \rho_w + (1 - \alpha_w)\, \rho_a \tag{1}$$

and

$$\mu_m = \alpha_w \mu_w + (1 - \alpha_w)\, \mu_a \tag{2}$$

where the indices w and a denote the properties of water and air, respectively. The variable α_w is defined as the volume fraction of water present in a specific cell. The surface tension force appears in the mixture momentum equation and is modelled using the *Continuum Surface Force* method, which was first published by Brackbill et al. (1992). A scalar transport equation is solved for α_w, which is expressed as follows (where the local mixture velocity is denoted with $\vec{U}$):

$$\frac{\partial \alpha_w}{\partial t} + \nabla \cdot \left(\alpha_w \vec{U} \right) + \nabla \cdot \left[\alpha_w \left(1 - \alpha_w \right) \vec{U}_{wa} \right] = 0. \tag{3}$$

In this equation, $\vec{U}_{wa}$ is a modelling parameter which physically represents a slip velocity between the water and the air, but is used in the model as an artificial compressive velocity. The flux related to $\vec{U}_{wa}$ in Equation (3) is modelled as the multiplication of an adjustment constant C_α and the flux related to the mixture velocity $\vec{U}$. Because it is crucial for numerical stability as well as for

physical feasibility that the variable α_w stays between 0 and 1, the solver applies the Multidimensional Universal Limiter for Explicit Solution (MULES) which combines a lower- and higher-order scheme for the calculation of the flux of the volume fraction. A more elaborate explanation can be found in the work of Damián (2013). Moreover, an air-water mixture is used in all simulations, but the flow properties change slightly between the different cases.

Finally, the Reynolds stresses which are a consequence of Reynolds-averaging the momentum equation, are calculated using a turbulence model. Turbulence modelling of bubbly flows is a complex matter, especially since the literature on the (modelling of) the interaction between bubbles and turbulence is inconclusive (Rensen et al. (2005)). Both bubble size (Gore and Crowe (1989)) and the number of bubbles (Mazzitelli et al. (2003)) might affect turbulence, making the turbulence spectrum possibly non-universal and dependent on the exact geometry and associated break-up and coalescence processes. Some authors propose to add specific source terms to the turbulence equations. Devolder et al. (2017) show that RANS models produce too much turbulent kinetic energy close to the free surface, which dampens the wave profile. Hence, a correction term is added to limit the turbulent kinetic energy close to the free surface. Emmerson et al. (2016) report that the $k - \epsilon$ turbulence model increases the turbulence generation at the interface between the phases, smearing the interface and dampening wave initiation. However, as Emmerson et al. (2016) do not propose correction terms to improve this model, it is unknown whether the same source terms as those engineered for free-surface flows have a positive effect on the flow behaviour in confined flows. Hu and Zhang (2007) include source terms in the k-ϵ model to incorporate the effects of interphase friction and flow resistance due to tube bundles in order to more accurately predict heat transfer in condensers, but the authors admit in their conclusion that the model needs improvement. Mirzabeygi and Zhang (2015) use a similar approach to model the increase in turbulence in the primary (gas) phase by assuming that the energy lost by a droplet (secondary phase) is converted into turbulent energy. Both studies employ an Eulerian-Eulerian approach and model the tube bundle as a porous medium, making it hard to convert the source terms to our Volume-Of-Fluid approach with well-defined tube walls. Furthermore, flow-induced forces which are of primary importance in this paper, are not investigated by Hu and Zhang (2007) and Mirzabeygi and Zhang (2015). Finally, most studies concerning two-phase flow in rod bundles and of which the primary research question is not related to turbulence modelling, do not mention the obtained or imposed turbulence quantities (Anglart and Nylund (1996); Sadek et al. (2018)) or do not even state which turbulence model is applied (Abbasian et al. (2015); Yu et al. (2019)). In conclusion, the literature does not present a straightforward way to modify single-phase turbulence models to two-phase flow applications. As the aim of this research is to investigate the influence of the phase distribution in the region of interest rather than turbulence modulation due to bubbles and as estimating the exact turbulent conditions is impossible without empirical data derived on the same geometry used in the case studies (as will be discussed further for each case separately), no changes are made to the single-phase k-ω

SST model (Menter (1994)) applied in this paper.

4. 5-by-3 tube bundle subjected to axial flow

The SBM which is described in Section 2 will now be applied to a case study comprising of the 5-by-3 tube bundle subjected to axial flow. The tube diameter and array pitch match the experiments of Liu et al. (2018) and Ren et al. (2018). The CFD simulation with the transient inlet condition defined by the new model is compared to the flow obtained from calculations using a steady air jet inlet boundary condition. The accuracy of the simulations is evaluated through comparison of the flow profile and of the force exerted on the central cylinder. Afterwards, the required computational time to complete the simulations is discussed.

4.1. Case description

The mixture flows from bottom to top and the vertically oriented tubes are placed in a square array. The surface mesh of the inlet boundary to be used in this analysis is shown in Figure 2 and contains 3,000 faces. The tube diameter is equal to 9.5mm whereas the pitch equals 12.6mm. The distance between the cell center of an outer cylinder and the nearest outer wall also equals the pitch, leading to a total length of 63mm in the x-direction and 37.8mm in the y-direction.

The axial length of the domain is 1.52m, subdivided in 600 equally large divisions. This leads to a total of 1,800,000 cells. In the SBM, the variables t_{unit}, m_g and Δt_{model} are set to 0.25s, 0.00005kg and 0.001s, respectively. Both phases enter the domain with velocity 1.5m/s. The parameters m_{min} and m_{max} equal 5% and 20% of m_g, respectively. The individual bubble parameters

In the cases with a steady inlet boundary condition, a precursor domain needs to be added in front of the actual computational domain to allow the steady air jets to break up into bubbles. While the precursor domain needs to be solved for every subsequent time step, use of the SBM allows the bubbles to enter the domain directly and therefore limits the computational effort of the flow simulation to the actual domain of interest. The SBM will be compared to two precursor domain simulations, where the domain was prolonged by 1m and 5m, respectively. The mesh is constructed in such a way that the axial length of the cells remains (almost) equal for all three cases, hence a total number of 3,000,000 cells is found when the precursor domain is 1m long and of 7,764,000 cells is obtained for the 5m long precursor domain. The boundary condition at the inlet of the precursor domain is shown in Figure 3 and consists of 6 steady air jets in a continuous water flow. Similar to the SBM, slip between the phases is not considered at the inlet: the inlet velocity is 1.5m/s.

The solver *interFoam* does not directly solve the flow equations for p. Instead, a theoretical scalar field p_{rgh} is obtained from the subtraction of the static pressure p and a hypothetical hydrostatic pressure field based on the

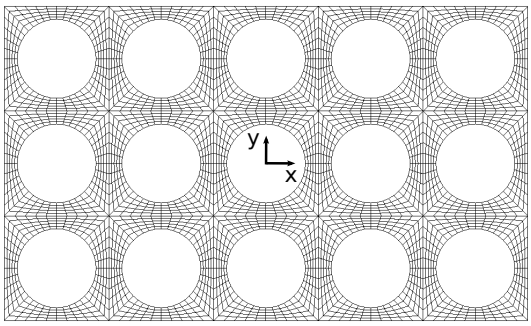

Figure 2: Mesh of the inlet boundary of the 5-by-3 tube bundle.

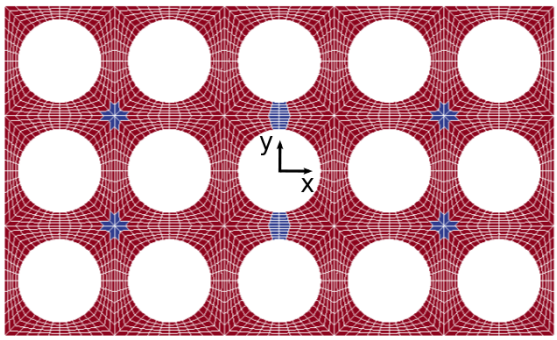

Figure 3: View of the steady boundary condition for α_w applied to the entrance of the precursor domain. The blue color indicates the presence of air, while water is shown in red. The mesh edges are shown in white.

local mixture density ρ_m. Concretely, the pressure field p_{rgh} is defined as:

$$p_{rgh} = p - \rho_m \vec{g} \cdot \vec{x}, \tag{4}$$

where $\vec{x}$ represents the position vector. At the outlet, the pressure p_{rgh} is set to atmospheric pressure. The gradient of the flow velocity U and of the volume fraction of water α_w are set to zero. Additionally, backflow at the outlet boundary is prohibited. A no-slip condition is applied to the cylinders' walls, i.e. zero velocity U and zero gradient condition for α_w and for the theoretical pressure p_{rgh}.

Liu et al. (2018) and Ren et al. (2018) do not report values of turbulent kinetic energy or dissipation rate. Consequently, it cannot be verified that the inlet conditions imposed on these variables are the same for the simulations and for the experimental case. This is not an issue as the main part of the discussion will be centred around the comparison of the numerical simulations with each other, as there are no empirical force spectra available either. The values of the turbulent flow properties k ($0.24\text{m}^2/\text{s}^2$) and ω (102.913s^{-1}) are imposed at the inlet in all simulations. A zero-gradient condition and wall functions are applied at the outlet and wall boundaries, respectively.

The density of water and air are set to 998.3 and 1.205kg/m^3, respectively. Kinematic viscosity of water and air are set to $1.00371\,10^{-6}$ and $1.511\,10^{-5}\text{m}^2/\text{s}$, respectively. Surface tension of the air-water interface is set to 0.07275N/m.

The scalar transport equation for α_w (Equation (3)) is split up in two substeps per time step, which are solved twice per time step. The iterative solution for α_w, U and the turbulence quantities employs a symmetric Gauss-Seidel smoother with a tolerance of 10^{-6}, whereas a preconditioned conjugate gradient (PCG) solver combined with a generalized algebraic multigrid (GAMG) preconditioner is used for p_{rgh}. The tolerance on the pressure is 10^{-5}. A second-order central discretization scheme is applied to all gradient and divergence terms, except for the divergence term in Equation (3) for which a Van Leer-scheme is used and the divergence terms containing k and ω, for which a second-order upwind scheme is used. For the pressure-velocity coupling, the PIMPLE-algorithm is used with 3 inner corrector loops and 2 outer corrector loops. The first order implicit Euler scheme is used to discretize the temporal derivatives. The time step in the CFD simulations is fixed to 10^{-4}s.

4.2. Results

The flow profile found over the first 0.23m of the actual domain (so downstream of the precursor domain if applicable) at a single time instant is shown in Figure 4, with the flow moving from bottom to top. The data presented here is the cell data, so every cell has a single colour. It is clear that a precursor domain of 1m does not allow the air jets to develop large bubbles able to create the forces obtained from the SBM. The outer jets have not broken up, but are prone to severe numerical diffusion as evidenced by the local value of $\alpha_w = 0.7 - 0.8$. The inner jet still contains cells completely filled with air ($\alpha_w = 0$) and exhibits some break-up into separate bubbles. Nevertheless, the break-up of the central

air jet is more pronounced if the flow is allowed to develop over a longer domain, e.g. in a precursor domain of 5m long. At the start of the actual domain, air bubbles have formed already. The difference between the steady inlet condition cases with precursor domain and the SBM is obvious: the SBM yields large bubbles, whereas in the case with the steady inlet condition only small bubbles appear and the water-air interface is smeared out due to numerical diffusion, although the size of the bubbles in the latter case is also related to the relatively small diameter chosen for the air jets.

Figure 5 depicts the real Fourier transform of the forces exerted on the central tube. For the simulation using the SBM, the temporal data used in the Fourier transform span 12s. In the steady inlet cases with a 1m- and 5m-long precursor domain, the force is calculated over 15s and 14.1s, respectively. Each time series was split into 4 parts, of which the Fourier transforms were calculated individually. The shown result is the average Fourier spectrum of the force.

Clearly, the force amplitude obtained from the shortest precursor domain simulation is lower than found in the other two cases. This is related to the absence of large bubbles and the strong diffusion of the air jets with little break-up inside the domain. On the other hand, if the precursor domain is taken sufficiently long, similar results between the SBM and the precursor domain simulation can be obtained, even though the low frequencies do not correspond completely because the bubbles formed in the precursor domain are not of the same size as those defined in the SBM. It is noteworthy that the energy contained in the lowest frequency range is higher in the y-direction than in the x-direction for the precursor domain simulations, due to the proximity of the jet to the central tube in the y-direction. This would not have been the case if the air jets were placed symmetrically around the central tube. The SBM does not exhibit a discrepancy between the x- and y-direction if the simulation time is sufficiently long.

One of the main objectives during the development of the SBM, was to make a time-efficient model with an accuracy equal or superior to that of a precursor model, but with less computational cost. The SBM prior to the CFD simulation took a total of 15,712s on a single core of a 2 x 12-core Intel E5-2680v3 (Haswell-EP @ 2.5 GHz) node in order to model a transient inlet over a time span of 15s. So, it takes an average of 1047s to model the inlet boundary condition for 1s of physical flow time. The subsequent CFD calculation was performed in parallel, on 120 cores (5 nodes of the same type); 12.0566s flow time was calculated in 259,026s. Hence, the CFD simulation takes 21,484s to calculate 1s of flow time. To calculate the computational time required to solve the flow equations in a precursor domain, it is assumed that the calculation time scales with the number of cells inside the precursor domain. The time required to calculate 1s of flow time in the actual 1.52m-long domain (i.e. 21,484s) is taken as a reference. This means that the time it takes to calculate 1s of flow time inside a precursor domain of 1m and 5m long on the same number and type of nodes amounts to 14,134s and 70,671s, respectively. Consequently, in order to determine the flow condition at the inlet of the actual domain, the SBM takes about 7.4% and 1.5% of the time required to do the same with a 1m-long

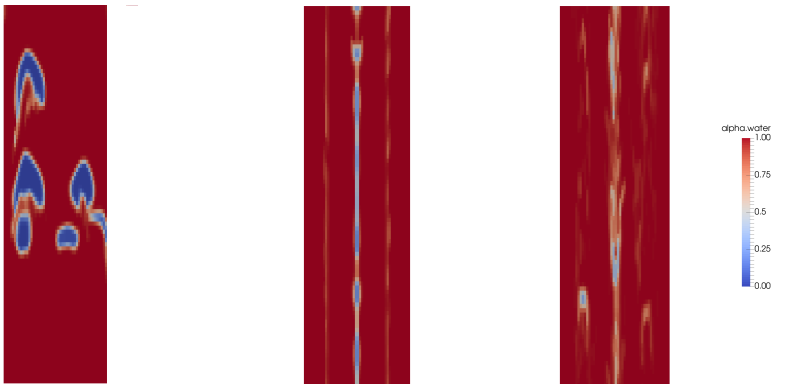

(a) (b) (c)

Figure 4: Contourplot of α_w obtained from the simulations with different inlet boundary conditions at a single time instant. The plane has a normal along the y-direction and is located in between the 3th and 4th row of cylinders. The first 0.23m of the actual domain are shown. The profile depicts cell data (no interpolation between adjacent cells is performed to get smoother profiles). The following cases are shown: (a) SBM, (b) steady air jets with a precursor domain of 1m long and (c) steady air jets with a precursor domain of 5m long.

and a 5m-long precursor domain, respectively. Increasing the number of cores naturally reduces the wall clock time required to perform the precursor domain simulation, which is not the case for the SBM which operates in serial. However, increasing the number of cores will probably not yield to a linear speed-up of the calculation and requires more computer infrastructure, which is why the SBM is still a valuable alternative. Additionally, the performance of the SBM could be increased by running parts of the code in parallel and by changing the brute force search algorithm currently used when defining a new bubble to e.g. a k-d tree model.

4.3. Final notes

Two additional comments can be made about the synthetic bubble model. Firstly, the SBM defines a boundary condition which is of stochastic nature. Moreover, as was noted in Section 2.2, some iterations in the model fail due to an inappropriate choice of the variables defining the bubble to be introduced in the pre-domain. The range of the stochastic variables, the number of cells in the pre-domain and the number of failed iterations depend on the values of the model parameters which are imposed by the user. Consequently, the computational time required to complete the model is dependent on the following model parameters: the time step used in the model Δt_{model}, the amount of air m_g introduced during a specific time interval t_{unit} and t_{unit} itself. The influence of these parameters on the model execution time is analyzed in Appendix A. Secondly, as noted in the introduction, it is well established that the predominant bubble shape appearing in a certain geometry is not necessarily spherical. At

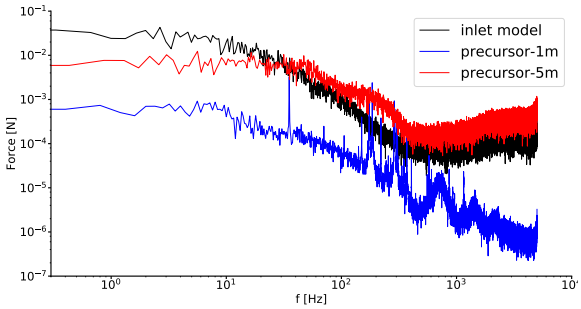

(a)

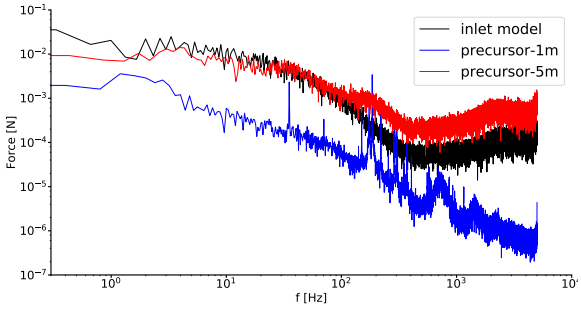

(b)

Figure 5: Real Fourier transform of the force profile on the central cylinder of the tube bundle extracted from the SBM simulation, the simulation with a precursor domain of 1m long and with a precursor domain of 5m long, respectively. Each time series was split into 4 parts, of which the Fourier transforms were calculated individually. The shown result is the average Fourier spectrum of the force (a) in the x-direction and (b) in the y-direction.

this point, only spherical bubble shapes have been implemented in the SBM, but the model was designed to allow easy insertion of other shapes. The model's flexibility goes even further, allowing non-uniform bubble size and location distributions, although these are not demonstrated in this paper because of the lack of knowledge about the physical bubble distribution occurring in the use cases presented here. However, empirically obtained bubble size distributions - for example with the method proposed by Gaillard et al. (2017) - can be introduced in the SBM in a rather straightforward manner. In cases where the bubble distribution is not a priori known and where there are indications that spherical bubbles are not an accurate approximation, the SBM could also be combined with a precursor domain, yielding a so-called "hybrid approach". In the hybrid approach, the SBM is applied at the inlet of a precursor domain in which the bubbles have the space to develop into a shape following from the solution of the flow equations. It is clear that the time gain in the hybrid approach compared to a full precursor domain simulation is more limited than the computational time reduction discussed in the 5-by-3 tube bundle, but the SBM will allow a shorter precursor domain length as break-up into separate bubbles does not have to occur (contrary to the situation with a steady inlet condition).

5. Tube bundle subjected to cross-flow

5.1. Introduction

Naturally, the SBM is not limited to tube bundles subjected to axial flow. There is a need for a transient inlet boundary condition in cross-flow applications as well. Kanizawa and Ribatski (2016) report the following flow patterns in a triangular (staggered) tube bundle subjected to upward two-phase flow: bubbles, large bubbles, dispersed bubbles, churn, intermittent and annular flow. In this paper, the air and water fluxes will be chosen such that churn flow is achieved. This flow regime can be modelled with the new SBM and the subsequent VOF-calculation. Moreover, the churn flow regime leads to potentially strong flow-induced forces on the cylinder wall, which can be compared to experimental data.

The number of studies about flow-induced vibration in a tube bundle below the fluid-elastic instability threshold is limited. A notable exception is the work by Zhang et al. (2007). They have shown that force fluctuations on the tubes can be linked to volume fraction profiles in the adjacent flow path. More specifically, it was concluded that lift fluctuations are linked to the vortex shedding in the wake of upstream cylinders, whereas drag fluctuations are linked to the volume fraction changes in the main flow, i.e. the occurrence of large air bubbles in intermittent or churn flow. The dominant frequency in the drag spectrum corresponds to the single peak in the pressure power spectral density (PSD) that de Kerret et al. (2017) have observed in churn flow as well. The dominant frequency of the lift force increases with increasing mixture velocity (Zhang et al. (2008) report an increase of frequency from 11Hz to 16Hz when doubling the gap velocity), whereas the dominant drag force frequency only

slightly changes from 4Hz to 4.625Hz over the same range. Contrariwise, the amplitude of both lift and drag forces is larger at higher flow velocities, which is confirmed by Álvarez Briceño et al. (2018). The geometry by Zhang et al. (2007) will be used as a starting point for the numerical analysis proposed here.

The goal in this case study is to reproduce the empirical results of Zhang et al. (2007) by modelling the flow using a VOF method combined with the SBM described in Section 2. The numerical aspects of this case are discussed in Section 5.2. The accuracy of the CFD simulations is evaluated on the basis of the force profile on the cylinders. The performance of the SBM is compared to steady-state inlet boundary conditions in Section 5.3. The flow field is analyzed in more detail in Section 5.4, where the close connection between the force profile and the volume fraction fluctuations will become clear.

5.2. Case description

As mentioned in the previous section, the numerical domain is based on the experimental set-up by Zhang et al. (2007). Firstly, the numerical domain and mesh are given. Secondly, the models used in the simulations will be discussed. Thirdly, the conditions imposed at the domain boundaries are explained in more detail, where the inlet condition is of particular importance. Fourthly, the definition of the Power Spectral Density (PSD) function is given.

The geometry consists of a row containing 6 full cylinders with diameter D equal to 38mm. In order to model the flow through a rotated triangular array, rows of half cylinders are positioned on either side of the full cylinders. The pitch P of the triangular array is 57mm, hence the ratio P/D equals 1.5. This yields a tube array with an axial length of $13P$. The inlet and outlet of the domain are extended with mesh sections with a respective length of $4P$ and $2P$ without cylinders. The complete domain is shown in Figure 6. The domain is two-dimensional. This simplification is supported by the work of Pettigrew et al. (2005) and Zhang et al. (2007). The structured mesh is constructed with maximal cell size of approximately 1mm^2. This results in a two-dimensional mesh containing 93,245 cells. A few details of the mesh are shown in Figure 7.

The density of water and air are set to 1000 and 1.2kg/m^3, respectively. The kinematic viscosity of water and air are set to 10^{-6} and $1.48\,10^{-5}\text{m}^2/\text{s}$, respectively. Surface tension of the air-water interface is set to 0.07N/m.

The simulations are performed in the open-source, finite volume package OpenFOAM® 6. Contrary to the previous case, no substepping is used in Equation (3), which is solved twice per time step by the MULES integrator. The iterative solution for both U and the turbulence quantities employs a symmetric Gauss-Seidel smoother with a tolerance of 10^{-6}. The same smoother is used for α_w, but with a tolerance of 10^{-8}. A preconditioned conjugate gradient (PCG) solver combined with a Diagonal Incomplete Cholesky (DIC) preconditioner is used for p_{rgh}. The tolerance on the pressure is 10^{-6}. A central discretization scheme is applied to all gradient terms. The divergence term in Equation (3) is discretized with a Van Leer-scheme, while the convective term and the divergence terms containing turbulence variables k and ω are discretized

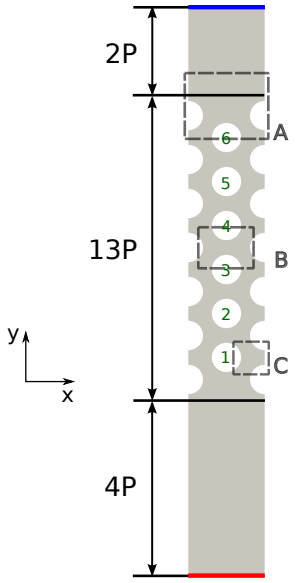

Figure 6: View of the numerical domain. The symbol P denotes the pitch of the tube array. The inlet and outlet boundary are shown in red and blue, respectively. The full cylinders are numbered in green in the direction of the flow (bottom-up).

with a second-order upwind scheme. The remaining divergence terms are centrally discretized. For the pressure-velocity coupling, the PIMPLE-algorithm is used with 3 inner corrector loops and 2 outer corrector loops. The first order implicit Euler scheme is used to discretize the temporal derivatives. An adjustable time step is used for all simulations, i.e. the time step is calculated automatically from the prerequisite that the maximal Courant number should not exceed 0.7. The forces are sampled with a frequency of 1kHz. The total simulated flow time equals 5s.

The SBM guarantees that a mass of air equal to 0.000315926kg (with a tolerance of 10^{-9}kg) is inserted during every time period of 1s, which equals the average homogeneous volume fraction of air of 80% found in the experiments. The time step used in the SBM Δt_{model} equals 0.001s. The inlet velocity is fixed at 1.667m/s. In order to evaluate the performance of the SBM, another case will be defined using a single stationary air jet positioned centrally at the inlet.

It is hypothesized that the forces and flow field obtained from the simulations with the SBM will be closer to the empirical data because the stationary air jets require more space to develop to large air bubbles seen in the experiments. As such, the inlet condition defined through the model is closer to the actual situation observed in the experiments than the stationary air jets, even though the exact bubble population or flow field is not known as a function of time.

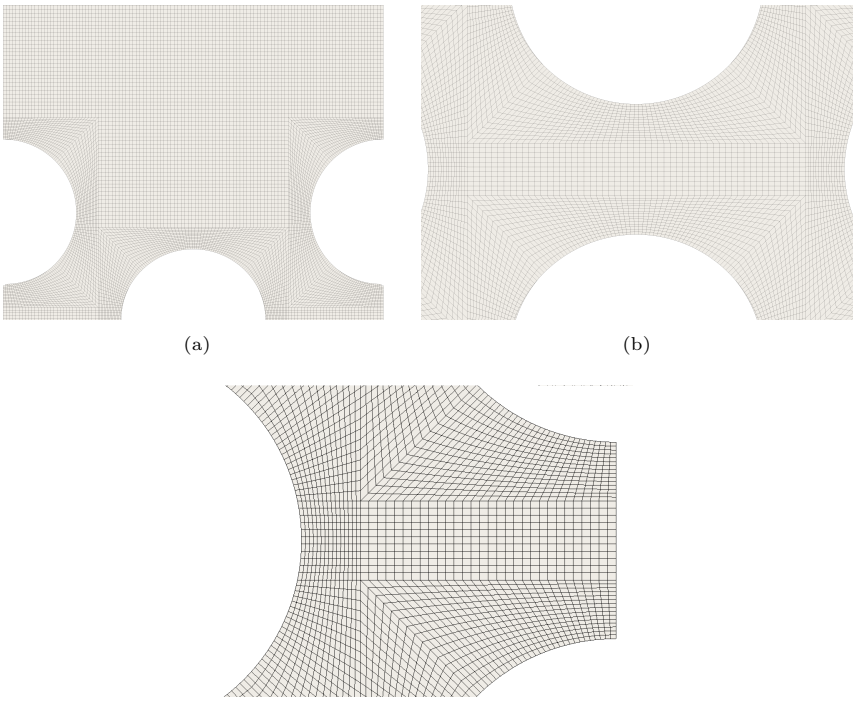

Figure 7: Details of the mesh used in the CFD simulations. The areas represented in detail here are indicated in Figure 6: (a) box A, (b) box B and (c) box C.

As highlighted in previous work (De Moerloose and Degroote (2020)), it is of vital importance to model the inlet as close to the experimental conditions as possible to obtain similar results.

At the outlet boundary - shown in blue in Figure 6 - the total pressure is set to atmospheric pressure. The gradient of the flow velocity U and of the volume fraction of water α_w are set to zero. Additionally, backflow at the outlet boundary is prohibited. A no-slip condition is applied to the cylinders' walls, i.e. zero velocity U and zero gradient condition for α_w and for the theoretical pressure p_{rgh}.

As mentioned before, the exact turbulent conditions at the inlet of the experimental set-up are not known. We have therefore imposed different turbulent intensities at the inlet of the tube subjected to cross-flow. Three simulations, with a turbulence intensity of resp. 1%, 5% and 10%, yield different turbulent intensity levels at the first cylinder, but the turbulence intensity at the fifth cylinder is very close for all three simulations (not shown). This indicates that the effect of inlet turbulence diminishes during flow through the array and has almost completely disappeared by the time the flow reaches the fifth cylinder. The turbulence creation and dissipation are linked to break-up and coalescence phenomena inside the tube bundle, generating a physical turbulence intensity independent of the turbulence level of the incoming flow. For all results discussed further in this paragraph, the values of the turbulent flow properties k and ω are imposed at the inlet based on a turbulent intensity of 10% and a mixing length of $0.07D_h$, with D_h being the hydraulic diameter of the inlet cross-section (9.128mm based on a normal depth of 0.019m which was extracted from the experimental setup). A zero-gradient condition and wall functions are applied at the outlet and wall boundaries, respectively.

In Section 5.3, the power spectral density (PSD) of the force on one of the tubes will be discussed in detail. This PSD is defined with Welch's method (Welch (1967)), which allows the reduction of unphysical power in the frequency domain due to the aperiodic nature of the time signal. In this method, the time range is subdivided in a number of segments with T time steps each. The force signal in time segment k is denoted by $f_k(n), k = 1..N$ and $n = 1..T$. Furthermore, a window function $w(n), n = 1..T$ is multiplied with the force in each time segment $f_k(n)$. If the Fourier transform of the time signal $f_k(n).w(n)$ is indicated with F_k, the PSD P_k over each time segment is calculated as follows:

$$P_k = \frac{|F_k|^2}{X}, \tag{5}$$

where X is given by:

$$X = \sum_{j=1}^{T} w^2(j). \tag{6}$$

Consecutive segments are not disjoint: a certain amount of overlap is desired in order to reduce the effect of the window function (if no overlap is used, some data points are neglected or at least reduced in importance). This is typically

expressed in a percentage, where 0% overlap corresponds to disjoint segments and 100% overlap would theoretically mean that all points are used in all segments. All PSD graphs presented in this work are constructed through Welch's method using the flat top window function (see Figure 8) with an overlap fraction of 80% and a frequency resolution of 0.5Hz. A resolution of 0.125Hz is reported by Zhang et al. (2008). Nonetheless, the current frequency resolution of 0.5Hz is sufficient for the purpose of this paper. Finally, the initial 0.5s of every simulation are not taken into account in the calculation of the PSD, as the two-phase flow has not yet reached the tube bundle by then and to remove any effect of the initialization of the flow field.

5.3. Force on the cylinders

As a way to evaluate the performance of the CFD simulations, the force profile on the wall of the first cylinder and the fifth cylinder in the array will be analyzed (indicated with a green number 1 and 5 in Figure 6, respectively). The water-air mixture flows from bottom to top, so cylinder 1 is the most upstream cylinder. It is expected that the force on this cylinder is highly affected by the incoming air bubbles. On the other hand, cylinder 5 is encountered far downstream in the tube bundle and is hence influenced by the wake of the previous cylinders as well as by the break-up of the incoming air structures. The force data will be evaluated in two distinct cases. The difference between both is in the inlet boundary condition: in the first case, the SBM is used to define a transient inlet profile whereas a stationary condition containing a single centrally positioned air jet is used in the second case. The average volume fraction of air entering the domain is 80%, but as the SBM has a stochastic character, the volume fraction as a function of time is not constant in that case.

Figure 9 shows the Fourier transform of the drag force on the first cylinder and on the fifth cylinder for the two different inlet boundary conditions. For the fifth cylinder, the experimental results published by Zhang et al. (2008) have been added for comparison. The SBM is clearly closest to the empirical spectrum, with the single-jet model severely overpredicting the most important low-frequent drag force components. This confirms the necessity of applying

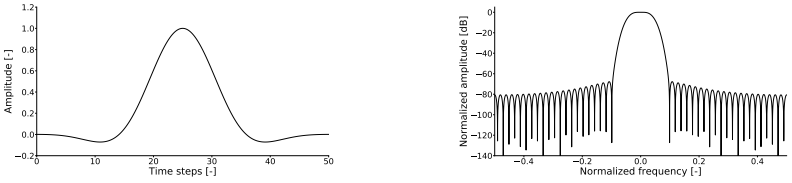

(a) (b)

Figure 8: View of the flat top window function (a) in the time domain and (b) in the frequency domain.

an inlet boundary condition close to the experimental conditions, even though these are not completely known. Furthermore, there is a clear harmonic content in the drag spectra obtained from the single-jet case. This is more pronounced for the first cylinder than for the fifth cylinder due to the previously mentioned break-up of the flow structures along the flow path through the tube bundle. The SBM, on the other hand, yields a more physical drag force spectrum with a rapid decrease in amplitude after the dominant peak at 9Hz. The drag spectrum exhibits peaks at 1.5Hz, 3Hz and 9Hz. A low frequency peak (at 2 Hz) was also observed by Zhang et al. (2009), but the authors stated that this peak is to be ignored. This statement was criticized by de Kerret et al. (2017) as this peak would be typical for the churn flow regimes. The dominant peak at 4-5Hz found in the experiments is not present in the simulation, but probably corresponds to the simulated force peak at 1.5-3Hz. The discrepancy between the SBM and the empirical data could be attributed to a potentially different bubble distribution found in the experimental set-up, which is not reported by Zhang et al. (2009).

Figure 10 shows the Fourier transform of the lift force on the first cylinder and on the fifth cylinder for the two different inlet boundary conditions. Compared to the respective drag force, the amplitude of the lift force is significantly smaller and the dominant peaks are less pronounced. The harmonic content of the single-jet case again proves that the flow is not modelled precisely in that case. The empirical spectrum indicates a single broad peak around 10Hz, whereas the SBM case yields a more narrow maximum at 9Hz. More generally, finding the correct lift force is more difficult than reproducing the drag. The reason for this is that the lift force is dependent on the wake dynamics, which is less dependent on the incoming flow structures, especially around the fifth cylinder. The largest difference in lift spectra between both simulations is found on the first cylinder. As the first cylinder does not experience a wake flow from an upstream tube, the lift force is probably created by an asymmetry in volume fraction between the left and right side of the cylinder. As the SBM creates distinct large air bubbles, this asymmetry is larger than in the stationary inlet condition case. This explains the difference in maximal values between both. However, the empirical force spectra on the first cylinder were not published.

5.4. Relating the force profile to the flow field

A representative view of the α_w-field is found in Figure 11 for the two aforementioned boundary conditions. In the first case (Figure 11a), necking of the air jet occurs due to a Kelvin-Helmholtz instability. The interface instability grows in amplitude until the air jet collapses at a certain point. Due to this collapse, a bubble is formed. After each necking occurrence, a pressure rise in the upstream air is observed. The pressure continues to rise until the resulting force on the superposed water layer is sufficient to form a water slug which is blown through the tube bundle. The remaining air in the jet is pushed further upwards by the incoming flow until a new instability arises on the air-water interface and the process is repeated. The drag force spectrum is severely influenced by the impact of the heavy water slugs. Due to the cyclic occurrence of

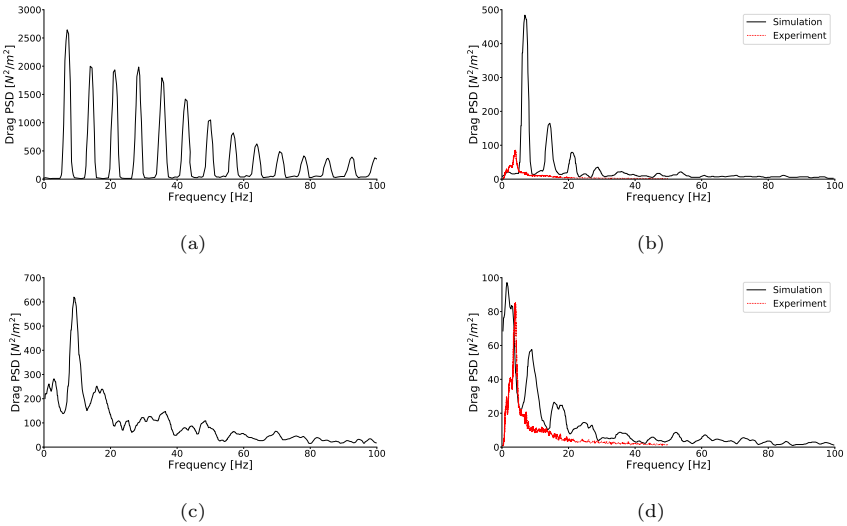

Figure 9: PSD of the drag force: on cylinder 1 (a) and 5 (b) with a single air jet at the inlet boundary and on cylinder 1 (c) and 5 (d) using the SBM.

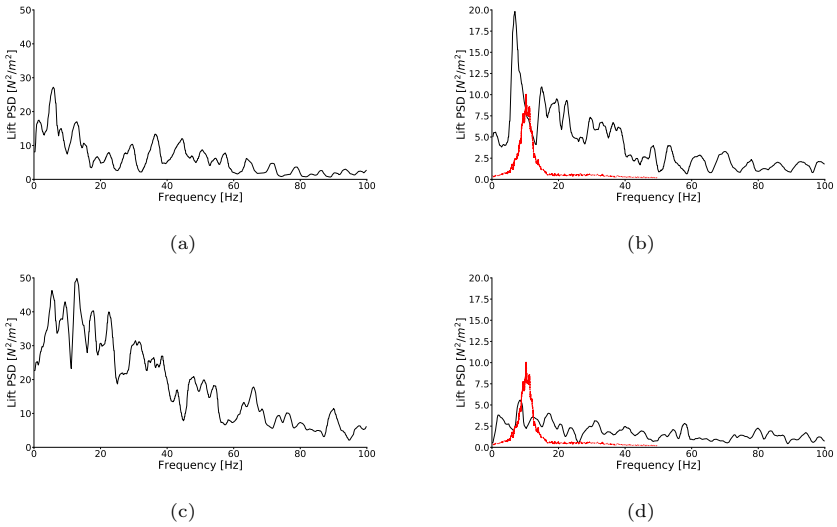

Figure 10: PSD of the lift force: on cylinder 1 (a) and 5 (b) with a single air jet at the inlet boundary and on cylinder 1 (c) and 5 (d) using the SBM.

necking, the tubes experience a cyclic force. This explains the strong harmonic nature of the drag force spectrum observed in Figure 9a. When the inlet is determined with the SBM, there is no air jet and therefore no cyclic jet collapse (see Figure 11b). The coalescence of large bubbles easily renders the incoming two-phase flow rather chaotic and aperiodic. Consequently, the force exerted on the wall exhibits a more noisy frequency response. This spectrum is potentially closer to reality if the incoming bubble sizes and shapes are consistent with the flow behaviour observed in the experiments. Presently, a clear dominant peak in the drag force spectrum (see Figure 9c) is observed without the harmonic content found in the stationary inlet cases, indicating that the SBM allows to predict the flow through the tube bundle more accurately.

Furthermore, it is visible that the water slugs break up rapidly inside the tube bundle. This creates a more bubbly-like flow in the tube bundle. In order to properly capture the interface with the VOF method, a finer mesh is needed. The accuracy of the force spectra will therefore decrease as the considered tube is positioned more downstream. This, however, is a property that is shared between all cases described above and is not related to the boundary condition imposed at the inlet. Nevertheless, the given mesh is sufficiently fine to calculate the average volume fraction of air inside the tube bundle with reasonable accuracy.

In order to verify this, the average α_w-field along a few radial lines will be compared to the empirically found phase distribution. These radial lines are shown in Figure 12. The corresponding value of $(1 - \alpha_w)$ is presented in Figure 13. These figures were obtained from the calculation with the transient inlet boundary condition defined with the SBM. The simulation results are shown in black, whereas the experimental results from Pettigrew et al. (2005) are shown in red. The volume fraction of air in the wake of the cylinders is overestimated by $15\% - 20\%$ in the simulations compared to the experimental results. The volume fraction profiles are overestimating the volumetric amount of air around the fifth cylinder with 15 - 20% compared to the empirical values. This discrepancy could be the result of the underestimation of the slip between the phases. In the simulations, no slip is modelled at the inlet and the flow is given little space to properly develop slip whereas a mixer is installed in the larger inlet domain in the experiments to let the flow develop before reaching the tube bundle. The value of the slip found in the experiments of Zhang et al. (2007) is not reported and therefore cannot be used as a point of comparison. However, we can use the findings described in other experimental studies on tube bundles subjected to air-water cross-flow to provide an estimation of the physical slip ratio, i.e. the ratio between the air and water velocities. Mitra et al. (2009) found that the void fraction in the tube bundle could be estimated using the drift-flux model. They found an average slip ratio of 2.65. Sasakawa et al. (2005) found an average slip ratio of 2.00 using void fraction measurements. In our simulations, the slip ratio on a cell basis is equal to 1 at any given time instant, as we apply the Volume-Of-Fluid method (this is a well-known drawback of any single-fluid approach). However, we can define the average air velocity in any cell of our domain by taking the time-average of the transient velocity value

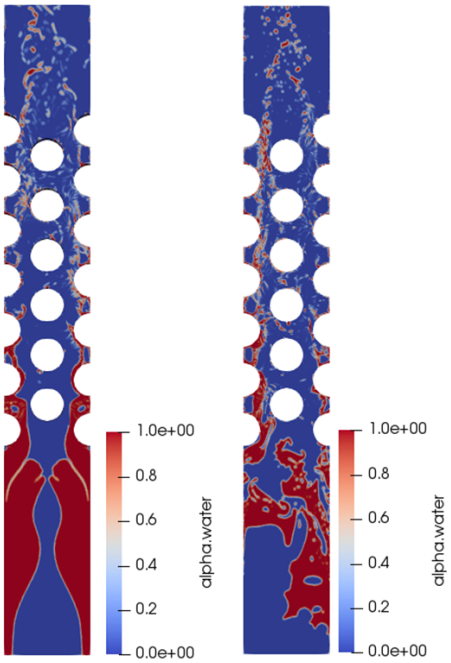

(a) (b)

Figure 11: Contourplot of the α_w-profile in the (a) single-jet case, (b) the case applying the SBM.

in the given cell, considering only the time instants when the volume fraction of air in the cell is at least 90%. The phase velocity of water can be defined in a similar manner. The slip ratios found over the four lines defined in Figure 12 are mostly between 0.7 and 1.6, so far below the empirical values. This probably explains the overestimation of the volume fraction of air in the simulations. More importantly, the general trends of the volume fraction distribution in the flow path are certainly comparable to the experimental results, showing that the main flow characteristics are modelled. Even though the amplitude might differ from experiments due to the overestimation of the volume fraction of air, the mechanism behind the oscillations and therefore also the frequency content of the force is well modelled.

6. Conclusion

An important parameter influencing the performance of Volume-Of-Fluid simulations of two-phase flows is the phase distribution in the region of interest. In this paper, the influence of the inlet condition is quantified by considering the flow-induced forces on tubes in an array. In two separate case studies, steady inlet conditions - consisting of one or multiple air jets surrounded by water - are compared to a transient inlet profile of stochastic nature. The latter is created by application of a novel inlet model, called the "Synthetic Bubble Model" (SBM), of which the algorithm is detailed in the paper.

In a first case study, the flow profile and the force exerted on the central rod in a 5-by-3 tube bundle subjected to axial flow as predicted by the SBM simulation and two precursor domain simulations are compared. The SBM and the simulation with the longest precursor domain yield similar results. However, the required simulation time in case of the SBM is about 24% of the simulation time of the precursor domain calculation. Hence, the simulation using the SBM is considerably less time-consuming than precursor domain simulations.

The second case study considers the flow field around a tube bundle in cross-flow was reproduced with good accuracy with the novel inlet condition and the subsequent Volume-Of-Fluid simulation. The SBM shows the best comparison to empirical force data (Zhang et al. (2007)) compared to a simulation with one stationary air jet. In this case, the SBM calculation requires a slightly longer computational time compared to the simulation with the steady boundary condition as no precursor domain was considered, but the extracted force profiles are clearly more accurate. Moreover, the empirical phase distribution (Pettigrew et al. (2005)) is reproduced using the SBM, although the volume fraction of air is slightly higher in the numerical case. Nonetheless, the present simulation in which the SBM is applied allows to predict the two-phase flow behaviour in a tube bundle subjected to churn/intermittent flow in a sufficiently precise way.

The presented use cases show the strong potential of the SBM using spherical bubbles and uniform probability distributions to determine the bubble size and location. In future work, empirically obtained bubble distributions can be introduced into the existing SBM in a straightforward manner to allow even more accurate predictions. Finally, if the appropriate bubble shapes are not

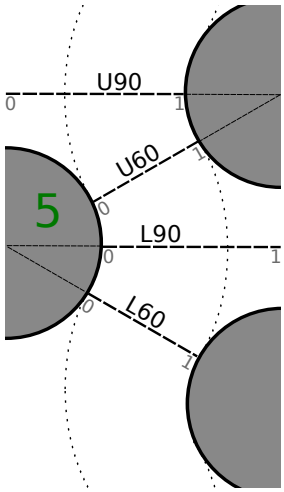

Figure 12: Schematic overview of the radial lines used in the analysis of the phase distribution. The radial lines are shown in dashed black lines, which are prolonged to the cylinder center with thinner dashed lines. The grey numbers indicate the normalized coordinate along each line. Cylinder 5 is indicated with the green number 5. The dotted lines show the theoretical mean flow path through the array.

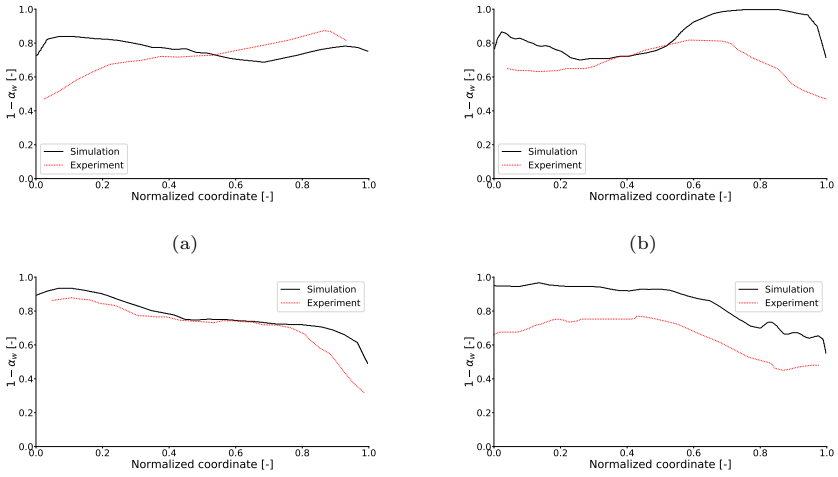

Figure 13: Time-averaged $(1-\alpha_w)$-profiles along the normalized coordinate on the radial line defined in Figure 12: (a) line L60, (b) line L90, (c) line U60 and (d) line U90.

known beforehand, one could consider a hybrid approach, applying the SBM to a (short) precursor domain in order to allow the bubbles to develop to their physical shape.

7. Acknowledgments

The authors gratefully acknowledge the funding by the Research Foundation-Flanders (FWO), Belgium, through the Ph.D. fellowship of Laurent De Moerloose. The computational resources (Stevin Supercomputer Infrastructure) and services used in this work were provided by the VSC (Flemish Supercomputer Center), funded by Ghent University, FWO and the Flemish Government department EWI.

8. References

References

Abbasian, F., Hadaller, G., Fortman, R., 2015. Single-phase and two-phase CFD simulations of the coolant flow inside a Bruce/Darlington CANDU flow channel. Proceedings of the 16th NURETH conference , 1–10.

Akiki, G., Jackson, T., Balachandar, S., 2017. Pairwise interaction extended point-particle model for a random array of monodisperse spheres. Journal of Fluid Mechanics 813, 882–928.

Alkhalidi, A., Amano, R., 2015. Factors affecting fine bubble creation and bubble size for activated sludge. Water and Environmental Journal 29, 105–113.

Anglart, H., Nylund, O., 1996. CFD application to prediction of void distribution in two-phase bubbly flows in rod bundles. Nuclear Engineering and Design 163, 81–98.

Brackbill, J., Kothe, D., Zemach, C., 1992. A continuum method for modeling surface tension. Journal of Computational Physics 100, 335–354.

Álvarez Briceño, R., Kanizawa, F., Ribatski, G., de Oliveira, L., 2018. Validation of turbulence induced vibration design guidelines in a normal triangular tube bundle during two-phase cross-flow. Journal of Fluids and Structures 76, 301–318.

Chesters, A., Hofman, G., 1982. Bubble coalescence in pure liquids. Applied Scientific Research 38, 353–361.

Damián, S.M., 2013. An extended mixture model for the simultaneous treatment of short and long scale interfaces. Ph.D. thesis. Universidad Nacional del Litoral.

de Kerret, F., Béguin, C., Etienne, S., 2017. Two-phase flow pattern identification in a tube bundle based on void fraction and pressure measurements, with emphasis on churn flow. International Journal of Multiphase Flow 94, 94–106.

De Moerloose, L., Degroote, J., 2020. A study of the vibration of a horizontal U-bend subjected to an internal upwards flowing air-water mixture. Journal of Fluids and Structures 93, 102883.

Denner, F., van Wachem, B., 2014. Fully-coupled balanced-force VOF framework for arbitrary meshes with least-squares curvature evaluation from volume fractions. Numerical Heat Transfer, Part B 65, 218–255.

Deshpande, S., Anumolu, L., Trujillo, M., 2012. Evaluating the performance of the two-phase flow solver interfoam. Computational Science & Discovery 5, 014016.

Devolder, B., Rauwoens, P., Troch, P., 2017. Application of a buoyancy-modified $k-\omega$ SST turbulence model to simulate wave run-up around a monopile subjected to regular waves using OpenFOAM. Coastal Engineering 125, 81–94.

Emmerson, P., Lewis, M., Barton, N., 2016. Influence of multiple bends for multiphase flow induced forces in 6" piping: measurements and CFD analysis. Proceedings of 11th International Conference on Flow-Induced Vibration , 1–5.

Gaillard, T., Roché, M., Honorez, C., Jumeau, M., Balan, A., Jedrzejczyk, C., Drenckhan, W., 2017. Controlled foam generation using cyclic diphasic flows through a constriction. International Journal of Multiphase Flow 96, 173–187.

Gore, R., Crowe, C., 1989. Effect of particle size on modulating turbulent intensity. International Journal of Multiphase Flow 15, 279–285.

Gouesbet, G., Berlemont, A., 1999. Eulerian and Lagrangian approaches for predicting the behaviour of discrete particles in turbulent flows. Progress in Energy and Combustion Science 25, 133–159.

Hirt, C., Nichols, B., 1981. Volume of Fluid (VOF) method for the dynamics of free boundaries. Journal of Computational Physics 39, 201–225.

Hu, H., Zhang, C., 2007. A modified k–ϵ turbulence model for the simulation of two-phase flow and heat transfer in condensers. International Journal of Heat and Mass Transfer 50, 1641–1648.

Kanizawa, F., Ribatski, G., 2016. Two-phase flow patterns across triangular tube bundles for air-water upward flow. International Journal of Multiphase Flow 80, 43–56.

Karnakov, P., Litvinov, S., Koumoutsakos, P., 2020. A hybrid particle volume-of-fluid method for curvature estimation in multiphase flows. International Journal of Multiphase Flow 125, 103209.

Larsen, B., Fuhrman, D., Roenby, J., 2019. Performance of interfoam on the simulation of progressive waves. Coastal Engineering Journal 61, 380–400.

Liu, H., Pan, L., Zhou, W., Ren, Q., Li, S., 2018. Axial development of gas-liquid flow regime maps in a vertical 5x5 rod bundle with prototypic spacer grids. Nuclear Engineering and Design 339, 1–10.

Mazzitelli, I., Lohse, D., Toschi, F., 2003. The effect of microbubbles on developed turbulence. Physics of Fluids 15, L5–L8.

Menter, F., 1994. Two-equation eddy-viscosity turbulence models for engineering applications. Industrial & Engineering Chemistry Research 32, 1598–1605.

Mirzabeygi, P., Zhang, C., 2015. Turbulence modeling for the two-phase flow and heat transfer in condensers. International Journal of Heat and Mass Transfer 89, 229–241.

Mitra, D., Dhir, V., Catton, I., 2009. Fluid-elastic instability in tube arrays subjected to air-water and steam-water cross-flow. Journal of Fluids and Structures 25, 1213–1235.

Nakamura, T., Fujita, K., Kawanishi, K., Yamaguchi, N., Tsuge, A., 1995. Study on the vibrational chracteristics of a tube array caused by two-phase flow. Part 1: random vibration. Journal of Fluids and Structures 9, 519–538.

Parmar, M., Haselbacher, A., Balachandar, S., 2010. Improved drag correlation for spheres and application to shock-tube experiments. AIAA Journal 48, 1273–1276.

Pettigrew, M., Zhang, C., Mureithi, N., Pamfil, D., 2005. Detailed flow and force measurements in a rotated triangular tube bundle subjected to two-phase cross-flow. Journal of Fluids and Structures 20, 567–575.

Ren, Q., Zhou, W., Du, S., Li, Z., Pan, L., 2018. Sub-channel flow regime maps in vertical rod bundles with spacer grids. International Journal of Heat and Mass Transfer 122, 1138–1152.

Rensen, J., Luther, S., Lohse, D., 2005. The effect of bubbles on developed turbulence. Journal of Fluid Mechanics 538, 153–187.

Sadek, O., Mohany, A., Hassan, M., 2018. Numerical investigation of the cross flow fluidelastic forces of two-phase flow in tube bundle. Journal of Fluids and Structures 79, 171–186.

Sasakawa, T., Serizawa, A., Kawara, Z., 2005. Fluid-elastic vibration in two-phase cross-flow. Experimental Thermal and Fluid Science 29, 403–413.

Selima, Y., Hassan, M., Mohany, A., Al-Hamadani, M., 2018. A model for fluidelastic instability in tube bundles subjected to two phase flow. Proceedings of the 9th International Symposium on Fluid-Structure Interactions, Flow-Sound Interactions, Flow-Induced Vibration and Noise 1, 1–7.

Shuard, A., Mahmud, H., King, A., 2016. Comparison of two-phase pipe flow in OpenFOAM with a mechanistic model. IOP Conference Series: Materials Science and Engineering 121, 012018.

Trapp, J., 1993. A discrete particle model for bubble-slug two-phase flows. Journal of Computational Physics 107, 367–377.

Welch, P., 1967. The use of Fast Fourier Transform for the estimation of power spectra: a method based on time averaging over short, modified periodograms. IEEE Transactions on Audio and Electroacoustics 15, 70–73.

Yu, S., Chen, J., Mi, X., Lu, L., Ding, G., Ding, C., 2019. Experimental and numerical investigation of two-phase flow outside tube bundle of liquefied natural gas spiral wound heat exchangers under offshore conditions. Applied Thermal Engineering 152, 103–112.

Zhang, C., Mureithi, N., Pettigrew, M., 2008. Development of models correlating vibration excitation forces to dynamic characteristics of two-phase flow in a tube bundle. International Journal of Multiphase Flow 34, 1048–1057.

Zhang, C., Pettigrew, M., Mureithi, N., 2007. Vibration excitation force measurements in a rotated triangular tube bundle subjected to two-phase cross flow. Journal of Pressure Vessel Technology 129, 21–27.

Zhang, C., Pettigrew, M., Mureithi, N., 2009. Further study of quasiperiodic vibration excitation forces in rotated triangular tube bundles subjected to two-phase cross flow. Journal of Pressure Vessel Technology 131, 1–8.

Appendix A. Influence of the model parameters on the modelling time

As the SBM is of stochastic nature, some iterations in Algorithm 1 fail. Running the model multiple times on the same case with the same parameter settings can yield slightly different results in terms of required computational time. Consequently, all datapoints discussed in this section represent the average duration over three runs. This average time includes only the execution of the SBM. The error bars on each figure represent the maximal deviation found in those three specific runs and are plotted symmetrically with respect to the average value. Overall, the average relative deviation of each simulation with respect to the corresponding average duration for its specific settings is 10.1%.

Firstly, the influence of Δt_{model} is analyzed. The dependence of the modelling time on Δt_{model} is straightforward: doubling Δt_{model} leads to half the number of positions in time to be modelled. Each iteration in Algorithm 1 then

also takes half the time to complete. Therefore, it can be concluded that the modelling time is inversely proportional to Δt_{model}.

Secondly, the elapsed time is plotted with respect to the variable m_g in Figure A.14, for $\Delta t_{model} = 0.001$s and $t_{unit} = 0.25$s. With increasing m_g, the computational time for the model increases superlinearly. This is due to the increased number of failed iterations. Clearly, this is a drawback to the current model which could be reduced by implementing a better search algorithm instead of the brute force search that happens during every iteration. This would not alter the superlinear behaviour shown in Figure A.14, but would significantly reduce the elapsed time for all datapoints.

Thirdly, Figure A.15 shows the modelling time as a function of t_{unit}, for constant $m_g/t_{unit} = 0.0002$kg/s and $\Delta t_{model} = 0.001$s. The reason for keeping the ratio m_g/t_{unit} constant instead of m_g is that the number of failed iterations depends on both parameters and this behaviour has already been discussed when analyzing Figure A.14. Probably, a decrease in t_{unit} (and therefore of available spots to place a new bubble) would result in more failed iterations similar to an increase in m_g. By keeping the ratio m_g/t_{unit} constant, the number of failed iterations relative to the number of successful iterations is hypothesized to be constant for all datapoints in Figure A.15, at least on average. Also note that the y-scale in Figure A.15 spans a significantly smaller range than in Figure A.14, showing that the elapsed time does not heavily depend on t_{unit}, as long as the ratio m_g/t_{unit} remains constant. The smaller modelling time found for the lowest value of t_{unit} could be explained by the fact that, per iteration, only one eighth of the total number of bubble positions needs to be evaluated (as t_{unit} is one eighth of the total flow time to be simulated). Possibly this allows for more efficient memory management during the run of the Python code.

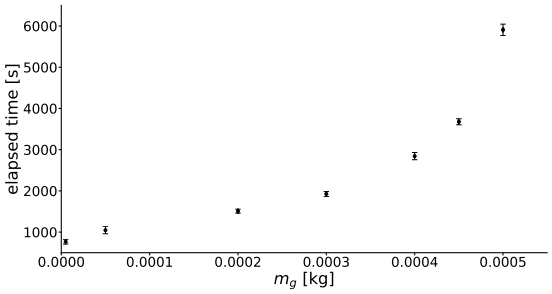

Figure A.14: Required time to complete the SBM as a function of the mass of air to be introduced m_g. For all datapoints, $\Delta t_{model} = 0.001$s and $t_{unit} = 0.25$s.

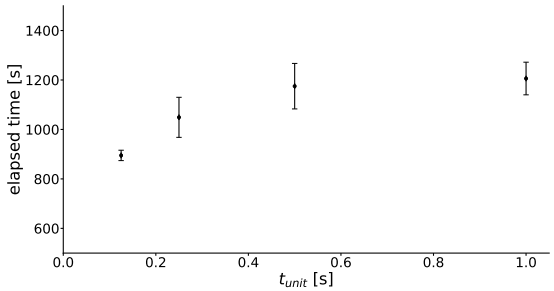

Figure A.15: Required time to complete the SBM as a function of the time interval t_{unit}. For all datapoints, $m_g/t_{unit} = 0.0002$kg/s and $\Delta t_{model} = 0.001$s.